Lattice dynamics, dielectric properties and structural instabilities of SrTiO$_3$ and BaTiO$_3$

Lattice dynamics, dielectric properties and structural instabilities of SrTiO$_3$ and BaTiO$_3$

Thomas Trautmann and Claus Falter

Institut für Festkörpertheorie, Universität Münster, Wilhelm-Klemm-Straße 10, 48149 Münster, Germany

E-mail: Falter@nwz.uni-muenster.de

Abstract

We extend our linear response description of materials with a strong ionic component of the electronic structure, previously applied successfully to the lattice dynamics, electron–phonon interaction and dielectric properties of the high-temperature superconductors (HTSC), to SrTiO$_3$ and BaTiO$_3$ which crystallize in the (perovskite) parent structure of the HTSC. Besides phonon-induced localized polarization processes at the ions in the form of dipole fluctuations, calculated with a modified Sternheimer method, which are typical for the ionic component of binding, on-site and off-site charge fluctuations modelling a charge flow along the Ti–O axis prove to be important. The latter delocalized polarization processes related to the covalent component of binding are introduced in our modelling to simulate changes of the hybridization between O 2p and Ti 3d orbitals under atomic displacements. Altogether, we obtain a reasonable description of the phonon dispersion and the dielectric properties of both materials, including the anomalous Born effective charges and the macroscopic dielectric constant. Moreover, comparative investigations within our microscopic model provide physical insight into the ferroelectric (FE) phase transition of BaTiO$_3$ and the antiferrodistortive (AFD) transition of SrTiO$_3$.

1. Introduction

In this paper we investigate the phonon dynamics, the structural instabilities, via soft modes, and the dielectric properties of the perovskite oxides SrTiO$_3$ and BaTiO$_3$. In particular, the lattice instabilities found in the perovskite structure, which is the parent structure of the high-temperature superconductors (HTSC), are responsible for many of their characteristic properties such as the temperature dependent ferroelectric (FE) and antiferrodistortive (AFD) phase transitions.

First-principles phonon calculations for the perovskites away from the zone centre, using density-functional perturbation theory (DFPT), have been performed for only a few compounds; see [1] and references therein. Here, we use for the calculation of the complete phonon dispersion and also the other quantities presented in this paper a previously proposed approximate modelling of the linear response and lattice dynamics, already applied successfully to the HTSC [2–5]. While this formalism is not fully *ab initio* and some analytic input is needed, it allows for physically motivated approximations on a microscopic level and for the investigation of their effects on the calculated properties. Also, the numerical calculations are far less time-consuming than for a full *ab initio* procedure in the framework of density-functional theory (DFT). Moreover, an extension to a non-adiabatic charge response, which has been proved to be essential for the investigation of the c-axis charge response coupled to the lattice in the HTSC [6], can be implemented directly. This is not possible for investigations in the framework of DFT which rely on the adiabatic approximation. The latter approximation, however, is sufficient for the calculated properties of the materials studied in this paper.

In our previous calculations of the lattice dynamics, electron–phonon interaction (EPI) and dielectric properties of the HTSC two basic electronic polarization mechanisms have been found to be important. These arise from the prevailing localized electronic structure of that predominant ionic compounds. Accordingly we find that phonon-induced polarization processes via ionic charge fluctuations, CF, are essential in particular for the ions in the CuO plane which lead to a charge transfer between these ions (delocalized mechanism). On the other hand, predominantly in the ionic layers, anisotropic dipole fluctuations, DF, localized at the ions become important (localized mechanism). In the present paper the effects of both of these polarization mechanisms and their interplay in generating the total polarization under atomic displacements are studied by calculating the phonon dispersion, the Born (transverse) effective charges Z^T, the high-frequency dielectric constant ε_∞ and, of course, the dynamical lattice instabilities in SrTiO$_3$ and BaTiO$_3$.

What has been discussed in the literature in context with the calculation of the anomalous large transverse charges Z^T of the ABO$_3$ perovskite compounds is that these dynamical charges are due in principle to both kinds of polarization mechanisms, localized as well as delocalized; see [7] and references therein. This has been achieved by a band-by-band decomposition of Z^T performed in DFT and shows that when the orbitals which interact are located on different atoms a substantial contribution to the anomalous charges is obtained via off-site hybridization. In this case the changes of hybridization under atomic displacements can be visualized as a charge transfer between the corresponding ions. In our modelling, such a delocalized contribution to the polarizability is described by the displacement-induced CF, while the remaining changes of hybridization related to the interacting orbitals on the same ion, looking like a local polarizability, are modelled in our approach by the ionic DF. Note in this context that an empirical model such as the shell model, which does not explicitly include transfer of charges and covalency like the bond orbital model (BOM) [8], is able to reproduce correctly the magnitude of Z^T [9]. However, in empirical models, fitting to the experiments is always done, e.g. to reproduce correctly the split between the longitudinal optic (LO) and the transverse optic (TO) modes at the centre of the Brillouin zone. In this way, for example in the shell model, covalency effects are implicitly introduced. Thus, quite generally in empirical modelling no suitable reference system can be defined as a starting point from which the relevant polarization processes can be studied explicitly and unambiguously. So, what may show up as an unusual large localized dipole polarizability of the oxygen ions in the shell model may appear as a delocalized charge transfer between the Ti and O ions in the BOM. In reality both kinds of polarization processes will be excited under atomic displacements in the crystal and we discuss in this paper in terms of CF and DF explicitly their influence not

only on the transverse charges and the macroscopic dielectric constant, but also in detail on the lattice dynamics and in particular on the lattice instabilities, using an *ab initio* rigid ion model (RIM) as an unprejudiced reference system, which does not include the polarization effects to be investigated.

In section 2 we briefly outline the theory and modelling of the density response, lattice dynamics and dielectric properties previously developed. Section 3 contains the model calculations for the phonon dispersion, lattice instabilities and dielectric properties of SrTiO$_3$ and BaTiO$_3$. Starting with the RIM, the influences of CF and DF are investigated. Finally, from a simultaneous comparison of the calculated results for the phonon frequencies, the transverse charges and the dielectric constant with the experimental data, an optimal modelling of the interplay of localized polarization effects in terms of DF and delocalized polarization effects via CF is proposed within our approach. Section 4 summarizes our results.

2. Outline of the theory and modelling

In section 2 a review of the theory and modelling will be given. Such a microscopic linear response approach is well suited for systems with a strong component of ionic binding and has been applied successfully to classical ionic crystals and high-temperature superconductors (HTSC) in the past. Details of the method can be found in [2, 10].

2.1. The reference system—rigid charge response

In order to investigate explicitly the influence of non-rigid electronic charge (CF) and dipole fluctuations (DF) on the phonon modes and dielectric properties an unbiased reference system without such electronic degrees of freedom is needed. This is achieved by an *ab initio* rigid ion model (RIM).

The basic assumptions underlying the RIM are adiabatic and harmonic approximations. The resulting dynamical matrix $t(\vec{q})$ can be split into a nuclear (ionic) part $t^I(\vec{q})$ and a (rigid) electronic part $t^E(\vec{q})$. $\vec{q}$ is a wavevector from the first Brillouin zone. The former is of purely long-range nature and can be calculated using the Ewald summation technique. The latter contains the long-range and short-range electronic parts and needs further approximations. Firstly, the electronic density ρ of the crystal is taken as a superposition of rigid ionic electron densities ρ_α:

$$\rho_\alpha(\vec{r}) = \sum_{\vec{a}\alpha} \rho_\alpha(\vec{r} - \vec{R}_\alpha^{\vec{a}}). \tag{1}$$

Here $\vec{a}$ and α are the indices of the Bravais and sublattices, respectively. This approximation is a suitable starting point for dominantly ionic crystals such as SrTiO$_3$ and BaTiO$_3$, in particular when ion softening in terms of effective (static) charges is taken into account to describe possible global covalence effects. Secondly, the electron density ρ_α of the single ions is treated as spherical symmetric, i.e. $\rho_\alpha(\vec{r}) = \rho_\alpha(r)$, and finally the total energy E of the system is approximated by a sum of ionic pair potentials $\phi_{\alpha\beta}$ and self-energies $E_\alpha^{\vec{a}}$ of the individual ions:

$$E(R) = \tfrac{1}{2}\sum_{\substack{\vec{a}\alpha \\ \vec{b}\beta}}{}' \phi_{\alpha\beta}(\vec{R}_\beta^{\vec{b}} - \vec{R}_\alpha^{\vec{a}}) + \sum_{\vec{a}\alpha} E_\alpha^{\vec{a}}, \tag{2}$$

where $R = \{\vec{R}_\alpha^{\vec{a}}\}$ denotes a given lattice configuration and the prime in equation (2) excludes the self-term $(\vec{a}\alpha) = (\vec{b}\beta)$. Thus, the RIM approximates the rigid, local part of the charge response and the EPI neglecting its non-rigid character, such as CF and DF, which will be investigated

in section 2.2 below. The corresponding dynamical matrix $[\vec{t}(\vec{q})]_{\text{RIM}}$ can be split into a long-range part, accounting for the long-range forces of both the ions and the electrons, and a short-range part (overlap forces) for the electrons. Whereas the former can be calculated with the help of the Ewald method, the latter is calculated using density-functional theory (DFT). For the correlation energy the parametrization in [11] has been used. The electron densities ρ_α of the individual ions are determined within the local density approximation (LDA) taking self-energy corrections (SIC) into account. For the oxygen anions, such as O^{2-}, the Kohn–Sham equations are made convergent by simulating the crystal environment using a Watson sphere potential with the depth of the Madelung potential. Global covalence effects are introduced into the RIM with the help of the concept of ion softening. Here, a tight-binding analysis of the (first-principles) electronic band structure supplies the (static) effective ionic charges as extracted from the orbital occupation numbers Q_μ of the μ (tight-binding) orbital:

$$Q_\mu = \frac{2}{N} \sum_{n\vec{k}} |C_{\mu n}(\vec{k})|^2. \tag{3}$$

$C_{\mu n}(\vec{k})$ stands for the μ component of the eigenvector of band n at wavevector $\vec{k}$ in the first Brillouin zone; the summation in equation (3) runs over all occupied states and N gives the number of elementary cells in the (periodic) crystal. All investigations in this paper are performed at the calculated ground state structure $R^0 = \{R_\alpha^{0\vec{a}}\}$ which is obtained by minimizing the crystal energy according to equation (2).

2.2. Modelling of the non-rigid charge response

The non-rigid part of the charge response under atomic displacements is modelled in linear response theory by electronic degrees of freedom (EDF) of charge fluctuation (CF) and dipole fluctuation (DF) type, respectively. Due to the *ab initio* character of the method this approach allows one to calculate all the electron–phonon and electron–electron coupling coefficients appearing in the model [2, 10], without any experimental input. Moreover, starting with the *ab initio* results of the coupling coefficients, which, of course, have been obtained using certain approximations, a parametrical variation of these microscopic well defined quantities may be useful for investigating selectively their influence on the phonon modes and the dielectric properties of the crystal in our model.

In our description the ionic densities $\rho_\alpha(\vec{r}, \zeta)$ perturbed by the ionic displacement are considered to depend on a set of EDF $\zeta = \{\zeta_\kappa^{\vec{a}}\}$ which, in turn, depend on the actual lattice configuration $R = \{R_\alpha^{\vec{a}}\}$; thus, $\zeta_\kappa^{\vec{a}} = \zeta_\kappa^{\vec{a}}(R)$. κ denotes the localization of the EDF in the elementary cell and is in predominantly ionic systems located at the ions. In the unperturbed ground state configuration, R^0, there will be no excitations of the EDF ($\zeta_\kappa^{\vec{a}}(R^0) = 0$). In the adiabatic approximation the dependence of the EDF on the ionic configuration is obtained from the minimization of the total energy $E(R, \zeta)$:

$$\frac{\partial E(R, \zeta)}{\partial \zeta} = 0. \tag{4}$$

Here $E(R, \zeta)$ is the modified crystal energy from equation (2), where $\phi_{\alpha\beta}$ and $E_\alpha^{\vec{a}}$ are now functionals of the perturbed densities $\rho_\alpha(\vec{r}, \zeta(R))$. In the harmonic approximation this finally results in a dynamical matrix

$$t_{ij}^{\alpha\beta}(\vec{q}) = \left[t_{ij}^{\alpha\beta}(\vec{q}) \right]_{\text{RIM}} - \frac{1}{\sqrt{M_\alpha M_\beta}} \sum_{\kappa,\kappa'} \left[B_i^{\kappa\alpha}(\vec{q}) \right]^* \left[C^{-1}(\vec{q}) \right]_{\kappa\kappa'} B_j^{\kappa'\beta}(\vec{q}). \tag{5}$$

The first term in equation (5) is the contribution from the RIM. M_α, M_β are the masses of the ions; i, j are Cartesian indices and κ, κ' run over the EDF in the elementary cell. The quantities

$\vec{B}(\vec{q})$ and $C(q)$ represent the Fourier transforms of the coupling coefficients as calculated from the crystal energy:

$$B_{\kappa\beta}^{\vec{a}\vec{b}} = \frac{\partial^2 E(R, \zeta)}{\partial \zeta_\kappa^{\vec{a}} \partial \vec{R}_\beta^{\vec{b}}} \tag{6}$$

and

$$C_{\kappa\kappa'}^{\vec{a}\vec{b}} = \frac{\partial^2 E(R, \zeta)}{\partial \zeta_\kappa^{\vec{a}} \partial \zeta_{\kappa'}^{\vec{b}}}. \tag{7}$$

The derivatives have to be performed at the ground state configuration R^0, i.e. $\zeta = 0$. B describes the coupling between the EDF and the atomic displacement (bare EPI) and C gives the mutual interaction between the EDF. Again, these quantities can be separated into a long-range and a short-range part; see e.g. [10]. Moreover, C can be decomposed into a kinetic one-particle contribution C^{kin} involving the electronic one-particle excitations (band structure) and a Hartree and exchange–correlation term $\tilde{V}$. Thus, C can be written as

$$C \equiv C^{\text{kin}} + \tilde{V} \equiv \Pi^{-1} + \tilde{V}, \tag{8}$$

where Π is the (irreducible) polarizability of the electronic system. The inverse of C needed in equation (5), i.e. the density response function (matrix), is finally given by

$$C^{-1} = \Pi(1 + \tilde{V}\Pi)^{-1} \equiv \Pi\varepsilon^{-1}, \tag{9}$$

with the dielectric function (matrix)

$$\varepsilon \equiv 1 + \tilde{V}\Pi. \tag{10}$$

Thus, the calculation of the interaction of the EDF has been expressed in terms of Π and $\tilde{V}$. In this work, two kinds of EDF are discussed. Firstly, charge fluctuations (CF) of a monopole character to describe a charge transfer under atomic displacements (delocalized mechanism). The set of CF are further divided into on-site CF: $\zeta_\kappa = Q_\kappa^{\text{on}}$ localized at the ions, which means that the occupation of the atomic orbital $\kappa = (n, 1)$ becomes a degree of freedom, and off-site CF: $\zeta_\kappa = Q_\kappa^{\text{off}}$. The latter may be located anywhere in the elementary cell outside of the ions, e.g. along the bond axis, in order to simulate the effect of the atomic displacements on the covalent part of a bond. On the other hand, the former describe the effect on the ionic component of binding. Secondly, we consider dipole fluctuations DF: $\zeta_\kappa = p_{\alpha i}$, in order to describe the phonon-induced localized polarization process at the ions (localized mechanism). In such an anisotropic non-rigid model, the electron density of an ion reads

$$\rho_\alpha(\vec{r}) = \rho_\alpha(r)|_{\text{RIM}} + \sum_\kappa Q_\kappa \rho_\kappa^{\text{CF}}(r) + \vec{p}_\alpha \cdot \hat{r} \rho_\alpha^{\text{D}}(r). \tag{11}$$

$\rho_\alpha(r)|_{\text{RIM}}$ is the density used in the RIM for the unperturbed ion following the latter rigidly. Q_κ and $\vec{p}_\alpha$ are the amplitudes, and $\rho_\kappa^{\text{CF}}(r)$ and $\rho_\alpha^{\text{D}}(r)$ the form factors of the CF and DF, respectively. $\hat{r}$ is a unit vector in the direction of $\vec{r}$. In the case of on-site CF the $\rho_\kappa^{\text{CF}}(r)$ are approximated by a spherical average of the orbital densities of the outer ionic shells calculated in LDA and taking SIC into account. For off-site CF a delta function is used. The dipole density $\rho_\alpha^{\text{D}}(r)$ is obtained from a modified Sternheimer method in the framework of LDA-SIC [10]. The on-site CF–CF submatrix of the matrix Π can be calculated approximatively from a tight-binding model of the electronic band structure [2, 5]:

$$\Pi_{\kappa\kappa'}(\vec{q}) = -\frac{2}{N} \sum_{\substack{nn' \\ \vec{k}}} \frac{f_{n'}(\vec{k} + \vec{q}) - f_n(\vec{k})}{E_{n'}(\vec{k} + \vec{q}) - E_n(\vec{k})} \left[C_{\kappa n}^*(\vec{k}) C_{\kappa n'}(\vec{k} + \vec{q}) \right] \left[C_{\kappa' n}^*(\vec{k}) C_{\kappa' n'}(\vec{k} + \vec{q}) \right]^*. \tag{12}$$

f, E and C are the occupation numbers, the electronic band structure and the expansion coefficients of the Bloch functions in terms of the tight-binding functions. When using also off-site CF in the model, the entire CF–CF submatrix of Π is calculated using a simplified parametrized model, sorting the Fourier transform:

$$\Pi_{\kappa\kappa'}(\vec{q}) = \sum_{\vec{a}} \Pi_{\kappa\kappa'}^{\vec{0}\vec{a}} \sum_{j=1}^{N_{\vec{a}}} e^{i\vec{q}(\vec{R}_{\kappa}^{\vec{n}_j} - \vec{\tau}_{\kappa'})} \tag{13}$$

into shells with increasing radius $|R_{\kappa'}^{\vec{a}} - \vec{\tau}_{\kappa'}|$. $\vec{\tau}_\kappa$ is the vector corresponding to the off-site CF located at sublattice κ. $N_{\vec{a}}$ denotes the number of Bravais vectors $\vec{R}^{\vec{n}_j}$ in the shell $\vec{a}$. Each shell has the same coefficient $\Pi_{\kappa\kappa'}^{\vec{0}\vec{a}}$. Finally, and very importantly, the coefficients $\Pi_{\kappa\kappa'}^{\vec{0}\vec{a}}$ in equation (13) must strictly obey a certain sum rule which holds for the charge response of an insulator [2]:

$$\sum_{\kappa'} \sum_{\vec{a}} N_{\vec{a}} \Pi_{\kappa\kappa'}^{\vec{0}\vec{a}} = 0. \tag{14}$$

2.3. Dielectric quantities

Within the framework of the above theoretical description of the electronic density response, an expression for the macroscopic (high-frequency) dielectric constant $\varepsilon_\infty(\hat{q})$, $\hat{q} = \vec{q}/q$, can be derived [5]:

$$\varepsilon_\infty(\hat{q}) = \lim_{\vec{q}\to\vec{0}} 1/[1 - v(q)\chi_0(\vec{q})], \tag{15}$$

with

$$v(q) = \frac{4\pi}{V_z q^2} \tag{16}$$

and

$$\chi_0(\vec{q}) = \sum_{\kappa,\kappa'} \rho_\kappa(\vec{q}) \left[C^{-1}(\vec{q}) \right]_{\kappa\kappa'} \rho_{\kappa'}^*(\vec{q}). \tag{17}$$

V_z denotes the volume of the elementary cell and $\rho_\kappa(\vec{q})$ is the Fourier transform of $\rho_\kappa^{CF}(r)$ and $\hat{r}\rho_\alpha^{D}(r)$, respectively. The transverse effective charges can be extracted in the long-wavelength limit from the equation

$$\hat{q} \cdot \underline{\underline{Z_\alpha^T}} \cdot \hat{q} = \lim_{\vec{q}\to\vec{0}} \left[\varepsilon_\infty(\hat{q}) \left[Z_\alpha + i\frac{\vec{q}}{q^2} \left(\sum_\kappa \rho_\kappa(\vec{q}) \vec{X}^{\kappa\alpha}(\vec{q}) \right) \right] \right]. \tag{18}$$

Z_α is the static charge of ion α, possibly taking ion softening into account. $\vec{X}^{\kappa\alpha}(\vec{q})$ describes the self-consistent reaction per unit displacement of the EDF as obtained in linear response theory and is given by

$$\vec{X}(\vec{q}) = \Pi(\vec{q})\varepsilon^{-1}(\vec{q})\vec{B}(\vec{q}) = C^{-1}(\vec{q})\vec{B}(\vec{q}). \tag{19}$$

In cubic symmetry the static dielectric constant ε_0 is calculated from the expression [5]

$$\varepsilon_0 = \varepsilon_\infty + \sum_\sigma \frac{\Omega^2(\sigma)}{\omega^2(\sigma)}. \tag{20}$$

ε_∞ is given in equation (15); σ runs over the optical modes at $\vec{q} \equiv \vec{0}$; $\omega(\sigma)$ are the frequencies of the TO modes and $\Omega^2(\sigma)$ the corresponding oscillator strengths, generally defined by the tensor

$$\Omega_{ij}^2(\sigma) = \frac{4\pi}{V_z} p_i(\sigma) p_j^*(\sigma), \tag{21}$$

which reduces for cubic symmetry to the scalar $\Omega^2(\sigma)$. In equation (21) the mode-induced electric dipole moments $p_i(\sigma)$ are defined by

$$p_i(\sigma) = \sum_{\alpha, j} Z_{\alpha, ij}^{\mathrm{T}} \frac{\tilde{e}_j^{\alpha}(\sigma)}{\sqrt{M_{\alpha}}}. \tag{22}$$

Here $\tilde{e}_i^{\alpha}(\sigma)$ denote the eigenvectors of the zero-wavevector optical modes, with eigenfrequency $\omega(\sigma)$, and $Z_{\alpha, ij}^{\mathrm{T}}$ is the tensor of the transverse effective charges from equation (18).

Finally, the amplitudes of the phonon-induced EDF in the mode $(\vec{q}\sigma)$ can be calculated from the expression

$$\delta\zeta_\kappa(\vec{q}\sigma) = \left[-\sum_{\alpha} \vec{X}^{\kappa\alpha}(\vec{q}) \cdot \vec{u}_{\alpha}(\vec{q}\sigma) \right] e^{i\vec{q}\cdot\tau_\kappa} \tag{23}$$

with the ionic displacements

$$\vec{u}_{\alpha}(\vec{q}\sigma) = \left(\frac{\hbar}{2M_{\alpha}\omega_{\sigma}(\vec{q})} \right)^{1/2} \vec{e}^{\alpha}(\vec{q}\sigma). \tag{24}$$

$\omega_{\sigma}(\vec{q})$ and $\vec{e}^{\alpha}(\vec{q}\sigma)$ are the eigenfrequencies and eigenvectors of the phonon modes $(\vec{q}\sigma)$.

3. Lattice dynamics, lattice instabilities and dielectric properties of SrTiO$_3$ and BaTiO$_3$

3.1. Results within the reference system (RIM)

In the cubic perovskite structure, BaTiO$_3$ passes through a ferroelectric (FE) phase transition as the temperature is lowered. SrTiO$_3$, which has the same high-temperature structure, behaves differently and an antiferrodistortive (AFD) transition is found as the temperature drops below about 105 K [12]. According to the soft mode theory of structural phase transitions the ferroelectric phase can be related to the high-temperature symmetric structure by the freezing in of an unstable TO zone-centre (Γ point) phonon, while the AFD transition is due to a softening of the lowest-frequency triply degenerate zone-corner R point mode [13]. Since the RIM has been derived within the harmonic approximation, this corresponds to a simulation at $T = 0$. Consequently, if the RIM were able to point to a FE transition, at least the results for BaTiO$_3$ should show an unstable mode ($\omega^2 < 0$) at the Γ point in the cubic structure, which, however, is not the case; see figure 1. In such a transverse optical (TO) ferroelectric mode the Ti ions move along one of the Ti–O bonds and the oxygens in the octahedra vibrate coherently in the opposite direction; see e.g. [1] and our calculations including CF and DF in later subsections. However, such an instability is not yet expected in the RIM due to the lack of a non-rigid charge response related to CF and DF which will be shown to lead to a destabilization of the ferroelectric mode (FEM).

Note that in this context it has been suggested that the FE transition is interrupted in SrTiO$_3$ due to quantum paraelectric behaviour, where the zero-point motion of the ions seems to suppress the long-range FE order [14–16]. So it is very interesting to investigate also the structural instabilities in SrTiO$_3$. Quite generally, the great sensitivity of ferroelectrics to chemical compositions, defects, pressure or electrical boundary conditions arises from a delicate balance between long-range Coulomb forces, favouring the FE state, and short-range overlap forces, favouring a non-polar structure [17].

Figures 1 and 2 display the results from using the RIM for BaTiO$_3$ and SrTiO$_3$, respectively, and no FE instability is found. The calculated phonon dispersion is given along the main symmetry directions $\Lambda \sim (1, 1, 1)$, $\Sigma \sim (1, 1, 0)$ and $\Delta \sim (0, 0, 1)$. Imaginary frequencies of unstable modes are plotted as negative numbers. From left to right the displacement patterns
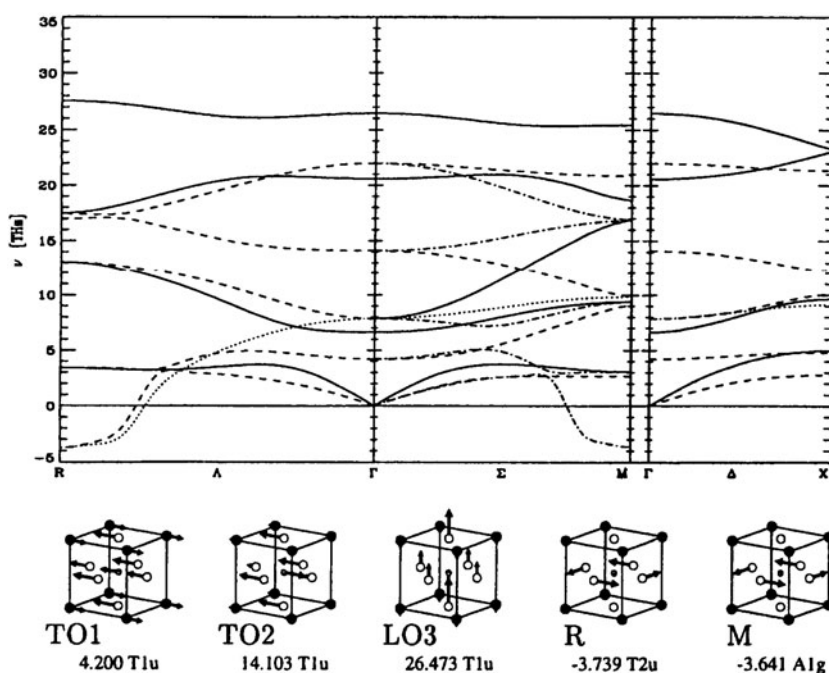
Figure 1. Calculated results within the RIM explained in the text for the phonon dispersion of BaTiO$_3$ along the main symmetry directions $\Lambda \sim (1, 1, 1)$, $\Sigma \sim (1, 1, 0)$ and $\Delta \sim (0, 0, 1)$ (model 1 in table 4). Imaginary frequencies of unstable modes are plotted as negative numbers. The classification of the phonon branches via irreducible representations has been managed in the figure by using different line types: Λ_1: ——; Λ_2: ·····; Λ_3: ———; Σ_1: ——; Σ_2: ·····; Σ_3———; Σ_4: —·—; Δ_1: ——; Δ_2: ·····; Δ_3: ———. Below the dispersion curves we have shown from left to right the two lowest TO modes, the highest LO mode and the two unstable modes at the R and M point.

in figures 1 and 2 are given for the two lowest TO modes, TO1 and TO2, the highest longitudinal optic (LO) mode, LO3, as well as the two unstable modes at the R and M points. The R point mode is the most unstable and already indicates an AFD transition in the RIM. In this mode the Sr and Ti ions do not move, while the oxygen octahedra rotate about one of the cubic axes passing through the Ti ion. The rotation is opposite in neighbouring elementary cells in all cubic directions. The other unstable mode at the M point is similar to the unstable R point mode, with the exception that the rotation of the octahedra is in the same sense in adjacent cells along the z-axis.

Due to the missing screening related to the non-rigid charge response in the RIM, the width of the phonon spectra in figures 1, 2 is too large. For example, the measured LO3 frequency for BaTiO$_3$ is 21.50 THz [18, 19] as compared with 26.47 THz in the RIM. For SrTiO$_3$ we have experimentally 23.83 THz [19, 20] and 31.82 THz in the RIM.

As already mentioned, the covalent character of the crystal can be taken into account globally via ion softening through (static) effective charges. There is considerable scattering in the results for these charges in the literature depending on the mode of definition (non-unique) and calculation [7]. As a general rule, partial covalence reduces the amplitude of the static effective charges in mixed ionic–covalent compounds (ion softening) because the charge transfer from the cations to the anions is not complete as in the entirely ionic case. The static effective charges for BaTiO$_3$ in table 1 are close to the first-principles results given in [7, 21].
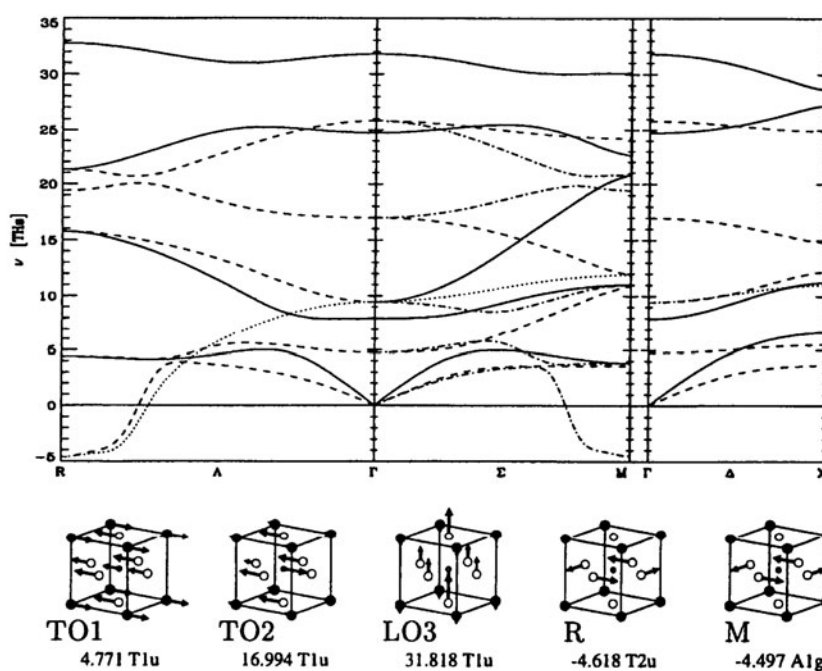
Figure 2. Results calculated within the RIM for the phonon dispersion of SrTiO$_3$ along the main symmetry directions as in figure 1 (model 1 in table 4).

Table 1. The first three columns show the static effective charges, rounded to two digits, as used in this work for SrTiO$_3$ and BaTiO$_3$. The next column (Mod) gives the resulting lattice constant in atomic units at minimized energy for these charges. The column headed TB contains the lattice constants at minimized energy for static effective charges as obtained from a tight-binding analysis of the electronic band structure [22, 23] and the column headed Exp displays the experimental results [21, 24].

	Static effective charges			Lattice constant (a/a_B)		
	Sr/Ba	Ti	O	Mod	Exp	TB
SrTiO$_3$	2.0	3.44	−1.81	7.26	7.38	7.50
BaTiO$_3$	2.0	2.87	−1.62	7.63	7.57	8.12

The larger ion softening for BaTiO$_3$ as compared with SrTiO$_3$ reduces the overlap repulsion and weakens the short-range forces, so the tendency towards ferroelectric behaviour should be increased in BaTiO$_3$.

For a reliable calculation of the phonon frequencies good structural data are very important. This is less likely if our calculated static effective charges from a tight-binding analysis of the electronic band structure according to equation (3) are used. For SrTiO$_3$ the tight-binding parameters given in [22] have been applied and for BaTiO$_3$ those given in [23]. The resulting lattice constants obtained using these charges in the minimization procedure for the crystal energy from equation (2) are listed in the last column of table 1. A better agreement with the experimental lattice constants of SrTiO$_3$ and BaTiO$_3$ is obtained for the set of static effective charges given in table 1. The magnitude of the latter is in the middle—between the results obtained from the TB analysis (TBA) and the purely ionic charges. These charges will be used in all the model calculations presented in this paper. More covalent charges,

Table 2. Dipole polarizabilities Π_α as calculated with the modified Sternheimer method [10] using the static effective charges from table 1.

	SrTiO$_3$			BaTiO$_3$		
	Sr	Ti	O	Ba	Ti	O
Π_α/a_B^3	5.67	1.72	13.96	10.52	2.25	13.63

such as those obtained from the TBA, turned out to yield unstable TO modes without any ferroelectric displacement pattern for both materials. This can be traced back to the fact that the long-range Coulomb forces favouring ferroelectricity are weakened too much with increasing ion softening. The favourable aspect of the long-range Coulomb interactions of driving a FE mode has been addressed in our modelling by simulations accounting for long-range pair potentials in equation (2) only. In such simulations we obtained for both materials an unstable TO mode with a FE displacement pattern. On the other hand, the simulations with exclusively long-range Coulomb forces increase the frequency of the rotational modes at the R and M points substantially. This leads to the conclusion that the AFD instability is driven by an increase of the short-range overlap forces. A cancellation between long-range Coulomb forces favouring the FE transition and short-range forces favouring the AFD transition is a fundamental characteristic of the perovskites; see also [21].

Finally, we remark that a ferroelectric-like pattern is seen in figures 1, 2 for the highest LO mode, LO3, and the second lowest TO mode, TO2. The lowest TO mode, TO1, however, does not show a FE mode pattern. Since the no-crossing theorem for modes belonging to the same irreducible representation forbids the TO2 mode from dipping below the TO1 mode, the ferroelectric instability can only be related to the TO1 mode. Therefore the TO1 mode is expected to take over the FE mode pattern when non-rigid contributions via CF and DF are introduced into the phonon-induced charge response. This problem will be investigated in the next two subsections.

3.2. The influence of dipole fluctuations

Two important ingredients are added to the investigation of the FE mode in this subsection. Firstly, starting from the reference system (RIM) presented in the last subsection, DF as a non-rigid electronic degree of freedom are additionally allowed for in the modelling. This means that on each ion the electrons may redistribute under atomic displacements in such a way that a varying dipole moment is induced on that ion. The latter is calculated with the help of the modified Sternheimer method within the LDA-SIC approach [10]. Thus no experimental evidence is taken as an input to the model. Secondly, the anisotropic environment of the oxygen ions is considered by taking into account an anisotropic dipole polarizability that is larger along the oxygen–titanium axis (O$_\parallel$ direction) than in the two directions perpendicular to this axis (O$_\perp$ direction). Such an anisotropy is consistent with the experimental and calculated values for the transverse charges Z^T for the oxygen which are considerably larger in the O$_\parallel$ direction than in the O$_\perp$ direction [7, 24]. Note that, recently, anisotropic DF also have been found important in our investigations of lattice dynamics and dielectric properties of the high-temperature superconductors, where the component parallel to the ionic c-direction perpendicular to the CuO planes dominates by far [5].

Table 2 contains the (isotropic) dipole polarizabilities Π_α calculated according to the Sternheimer method using the static effective charges of the RIM from table 1. The larger polarizability obtained for Ba as compared to Sr is due to its higher atomic number and the

Table 3. The data have been calculated on the basis of the reference model (*ab initio* RIM with static effective charges according to table 1) including additionally the (isotropic) dipole polarizabilities from table 2 (isotropic dipole model). The phonon frequencies ν are given in units of THz. The transverse charges Z_α^T and the macroscopic dielectric constant ε_∞ have been calculated according to equations (18) and (15), respectively.

	SrTiO$_3$	BaTiO$_3$
ν(TO1)	3.85	2.88
ν(LO3)	26.68	22.47
Z^T(Sr/Ba)	2.60	2.85
Z^T(Ti)	3.79	3.21
Z^T(O$_\parallel$)	−3.12	−2.52
Z^T(O$_\perp$)	−1.64	−1.77
ε_∞	3.15	3.06

Table 4. Comparison of the calculated results from three models discussed in the text for SrTiO$_3$ and BaTiO$_3$ for the phonon frequencies ν in THz, the transverse effective charges Z_α^T and the macroscopic dielectric constant ε_∞ with corresponding experimental values. Model 1 is the RIM reference model, model 2 includes anisotropic DF only and model 3 describes the final scenario with anisotropic DF and CF as screening processes. The experimental data for the phonon frequencies are from [18–20], those for Z_α^T from [24] and those for ε_∞ from [19]. Π_α denotes the dipole polarizability in units of a_B^{-3}, $\eta = \Pi_{O_\perp}/\Pi_{O_\parallel}$ is the ratio of the anisotropy for the oxygen polarizability and γ is a model parameter which describes the positions of the centres of the off-site CF; see figure 6. Imaginary frequencies of unstable modes are given as negative numbers.

	SrTiO$_3$			BaTiO$_3$			Experiment	
Model	1	2	3	1	2	3	SrTiO$_3$	BaTiO$_3$
ν(TO1)	4.77	−2.27	−2.73	4.20	−3.39	−5.35	—	—
ν(TO2)	16.99	5.13	5.22	14.10	3.29	3.40	5.25	5.43
ν(TO3)	25.83	22.92	19.97	22.00	19.59	16.17	16.34	14.60
ν(LO1)	7.95	4.90	5.03	6.64	3.29	3.35	5.13	5.40
ν(LO2)	24.76	16.56	14.36	20.58	13.54	12.47	14.21	14.03
ν(LO3)	31.82	26.63	23.81	26.47	22.16	18.38	23.83	21.50
Z^T(Sr/Ba)	2.00	2.09	2.46	2.00	2.38	2.64	2.4	2.9
Z^T(Ti)	3.44	6.58	5.53	2.87	6.03	5.44	7.0	6.7
Z^T(O$_\parallel$)	−1.81	−3.39	−4.04	−1.62	−2.87	−3.68	−5.8	−4.8
Z^T(O$_\perp$)	−1.81	−2.64	−1.97	−1.62	−2.77	−2.20	−1.8	−2.4
ε_∞	1.00	4.30	4.54	1.00	5.06	5.48	5.18	5.24
$\Pi_{O_\parallel}$	—	33	18.40	—	42	20.00	—	—
$\Pi_{O_\perp}$	—	11	13.96	—	14	13.63	—	—
η (%)	—	33.33	75.87	—	33.33	68.15	—	—
γ (%)	—	—	23.60	—	—	21.00	—	—

larger Ti polarizability of BaTiO$_3$ is consistent with a stronger electron transfer into the Ti 3d band in the case of BaTiO$_3$ as compared to SrTiO$_3$ leading to a stronger ion softening, as could be extracted from table 1. A calculation of the phonon dispersion of BaTiO$_3$ and SrTiO$_3$ using the dipole polarizabilities given in table 2 generates a global renormalization of the frequencies as compared with those of the ionic reference system displayed in figures 1 and 2, respectively, towards the experimental values. For example, the highest LO mode in SrTiO$_3$ is decreased from 31.82 THz in the RIM (figure 2) to 26.68 THz (table 3), which can be compared with the experimental value of 23.83 THz (table 4). In the case of BaTiO$_3$ we obtain a decrease from 26.47 in the RIM (figure 1) to 22.47 THz (table 3), while the experiments yield 21.50 THz
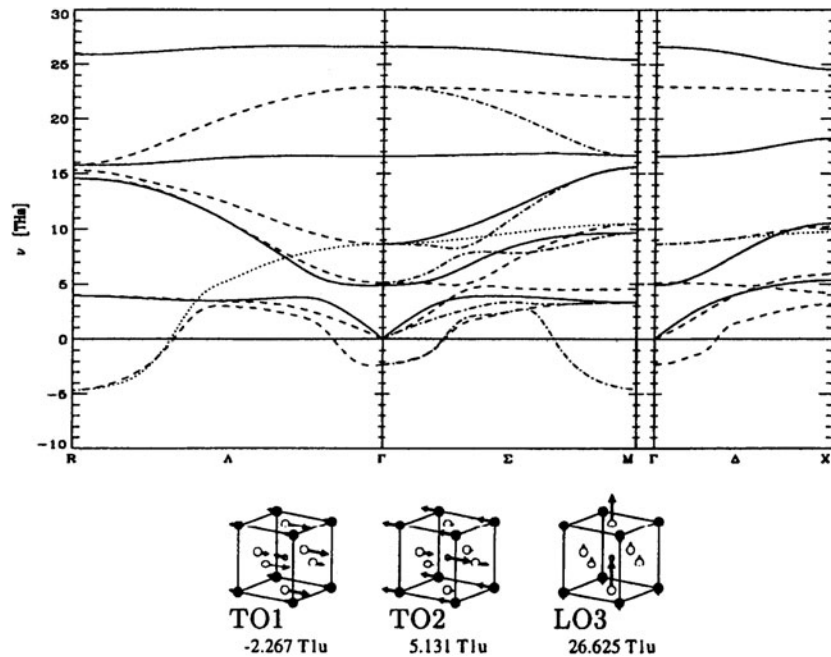
Figure 3. Calculated results for the phonon dispersion of SrTiO$_3$ along the main symmetry directions, as in figure 2, including additionally anisotropic dipole polarizabilities given by the ratio $\Pi_{O_\parallel}/\Pi_{O_\perp} = 33a_B^3/11a_B^3$ (model 2 in table 4).

(table 4). Moreover, we find that the lowest TO mode at Γ, TO1, is strongly renormalized; see figures 1 and 2 and table 3, respectively. However, TO1 does not become unstable at the Γ point and the TO1 displacement pattern does not yet take over the ferroelectric mode behaviour. Comparing the transverse charges, Z^T, in table 3 with the static charges in table 1, we have indications that the dipole polarizabilities might drive the model in the right direction. The transverse charges of oxygen display the correct anisotropy ($Z_{O_\parallel}^T > Z_{O_\perp}^T$) despite the isotropic dipole polarizability due to the anisotropic environment. However, the magnitudes of $Z^T(O_\parallel)$ are too small as compared to the experimental values given in table 4. The same is true for the calculated macroscopic dielectric constant ε_∞; see tables 3 and 4.

In order to investigate the influence of an anisotropic dipole polarizability on the FE mode, we treat the polarizabilities $\Pi_{O_\parallel}$ and $\Pi_{O_\perp}$ parallel and perpendicular to the O–Ti axis as free parameters. The results for the phonon dispersion of SrTiO$_3$ and BaTiO$_3$ are displayed in figures 3 and 4 and in table 4 (model 2). Only with unrealistic high polarizabilities for $\Pi_{O_\parallel}$ (compare the corresponding values in table 4 with those from the Sternheimer method in table 2) were we able to destabilize the TO1 mode causing it to show a FE mode pattern; see figures 3 and 4. The increased polarizability in the system is also reflected in the larger transverse charges, Z_α^T (table 4), which are a measure of the change of electronic polarization under ionic displacements (with zero macroscopic electric field). Moreover, ε_∞ is increased as compared to the isotropic case in table 3 and in better agreement with the experiment. An improved knowledge of Z_α^T and ε_∞ is also important for a better description of the long-range effect of the Coulomb interactions on the lattice dynamics of ionic crystals and directly related to the LO–TO splitting. Summarizing, in order to simulate a FE transition with DF only, an unrealistic large dipole polarizability $\Pi_{O_\parallel}$ had to be admitted. Even in this case, $Z^T(O_\parallel)$ and
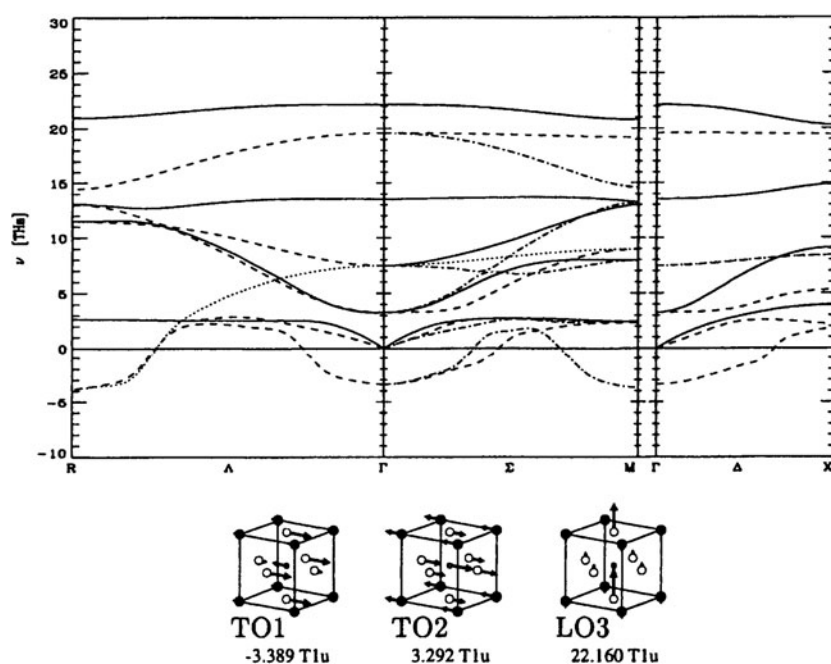
Figure 4. Calculated results for the phonon dispersion of BaTiO$_3$ along the main symmetry directions, as in figure 1, including additionally anisotropic dipole polarizabilities given by the ratio $\Pi_{O_\parallel}/\Pi_{O_\perp} = 42a_B^3/14a_B^3$ (model 2 in table 4).

ε_∞ are underestimated, suggesting a lack of other polarization processes. Thus, we conclude that the localized screening mechanism via DF, while favouring FE mode behaviour, should be supplemented by a delocalized mechanism, which in our microscopic modelling is realized in terms of CF. The role of CF in addition to DF is investigated in the next subsection.

3.3. The influence of charge fluctuations

According to section 2.2, CF are modelled as fluctuating charge centres located either at an atomic orbital with a certain form factor calculated in the LDA-SIC (on-site CF) and/or at any arbitrary point in the unit cell, e.g. on the Ti–O bond (off-site CF), with a δ-function as the form factor.

Before presenting the results of our simulations, some typical scenarios for a delocalized mechanism are considered in figure 5 from a qualitative point of view. Here five possible locations of CF (which can be considered to describe locations on the oxygen–titanium chain) are displayed. Figure 5(a) illustrates a purely covalent system with ionized atoms of the same kind. The horizontal arrows symbolize the displacements of the ions and the vertical arrows indicate the location of the CF centres at the middle of the bond axis. In this case, the region of compressed bonds gets more attractive for an electron (a vertical arrow down means an electron flow into the centre, $\delta Q_\kappa < 0$). Due to overall charge conservation these electrons have to come from the centre on the elongated bond (a vertical arrow up means an electron flow out of the centre, $\delta Q_\kappa > 0$). However, from the symmetry of the chain, the charge transfer (CT) has no unique direction, i.e. the CT in positive and negative directions along the chain are degenerate. This symmetry is broken by displacements in the partly ionic case shown
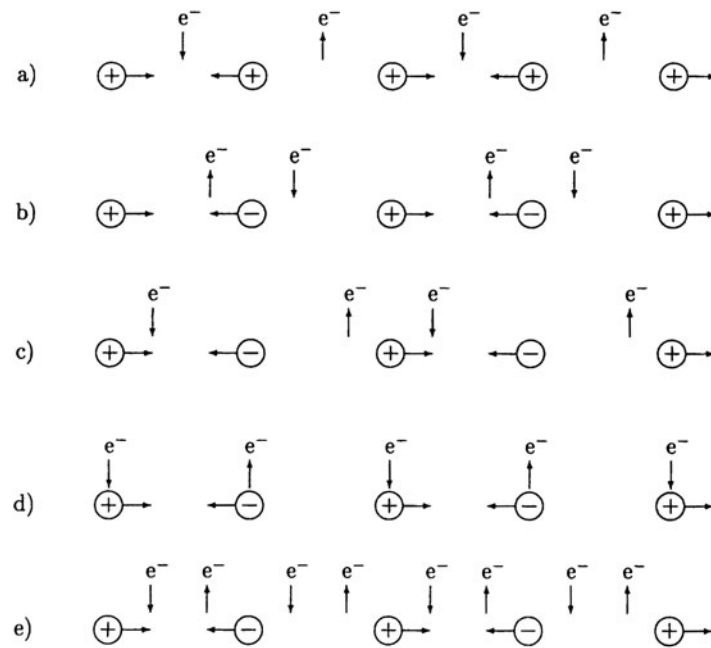
Figure 5. Various scenarios for locating charge fluctuations (CF) along the Ti–O chain as discussed in the text. Horizontal arrows indicate the displacements of the ions. Arrows pointing upward or downward, respectively, mean an electron flow away from ($\delta Q > 0$) or towards ($\delta Q < 0$) the location of the centre of the CF, respectively.

in figures 5(b)–(e), where positive and negative ions alternate, like in the Ti–O chain. Even without CF the rigid displacements of the ions, e.g. in the ferromode, result in a net electron shift in the direction of the displacement of the negative ion (e.g. oxygen). The direction of the CT resulting from the CF, however, is expected to depend on how closely the CF centres are located relative to the ions, say the oxygen and titanium ions. In figure 5(b) the CF centres are assumed to be located symmetrically close to the ground state position of the repulsive oxygen ion. This causes $\delta Q_\kappa > 0$ on the shorter bond. Since the electrons will pass via the attractive titanium ion in order to reach the centre of the elongated bond, the broken symmetry has lifted the degeneracy of the direction of the charge flow. Thus, the non-rigid phonon-induced electron flow is superposed in phase on the rigid charge shift of the oxygen ions in this case. This is expected to result in an increased change of polarization and correspondingly in a higher transverse charge, as found experimentally for $SrTiO_3$ and $BaTiO_3$. The opposite is true in the situation sketched in figure 5(c). Here, the CF centres are assumed to be symmetrically close to the attractive titanium ion. This results in $\delta Q_\kappa < 0$ on the compressed bond. Since, as in the previous case, the electrons are expected to pass via the attractive titanium ion to reach the centre of the shorter bond, the induced electron flow is out of phase with the rigid charge shift of the oxygen ion. As a consequence, the change in polarization on the transverse charges should decrease. From this reasoning it seems likely that a favourable situation for modelling an increase of the effective charges and a ferroelectric instability is generated by assuming the CF centres to be close to the oxygen ion like in figure 5(b). However, in such a model the electrons would move from the compressed bond into the elongated band, which is not realistic. Such a difficulty is not present in the models displayed in figures 5(d) and (e). In figure 5(d) only on-site CF centres located at the ions are involved. As a result, the electrons move along
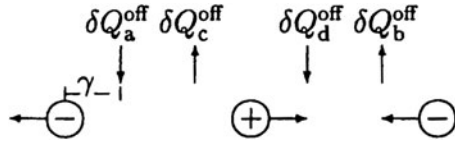
Figure 6. Localization of the off-site CF centres expressed by the quantity γ as discussed in the text. The arrows have the same meaning as in figure 5.

the shorter bond to the attractive titanium ions. However, from symmetry arguments it can be shown that on-site CF are not excited in the TO modes at the Γ point. Finally, figure 5(e) shows a simple solution to the problem. Here two CF centres are located on each bond. Analogously to the case in 5(b), this results in $\delta Q_\kappa > 0$ on the side where the displacement of the repulsive oxygen occurs. However, unlike the case in 5(b), the electrons do not have to move to the elongated bond; instead they are transferred to the centre close to the attractive titanium ion. Moreover, this non-rigid electron flow is in phase with the rigid charge shift of the oxygen, leading to an increase of the change of polarization. Note that the scale on which the CT takes place in direct space is an important factor for the magnitude of the displacement-induced changes of the polarizability and can be modelled by the location of the off-site centres with respect to the ions; see the parameter of localization γ in figure 6.

In the following, on-site and off-site CF will be modelled. On-site CF do not couple with the FE mode, but have an influence on phonon modes of other symmetry types and, of course, on the dielectric properties such as the macroscopic dielectric constant ε_∞ [5, 10]. A comparison between the specific influence of DF and CF on the FE instability is performed using a model constructed in parallel to figure 5(b) as far as the off-site CF centres are concerned. Then, a second model analogous to that of figure 5(e) will be investigated. While the numerical results obtained for both models are quite similar, model 5(e) should be preferred because it allows for a correct interpretation of the phonon-induced charge transport as discussed above.

The crucial parameter for the generation of a FE mode by DF in the last subsection was the size of the anisotropy of the dipole polarizability. The latter will be measured by the ratio

$$\eta = \frac{\Pi_{O_\perp}}{\Pi_{O_\parallel}}, \tag{25}$$

with $\Pi_{O_\perp}$ and $\Pi_{O_\parallel}$ the polarizabilities of oxygen in the directions perpendicular and parallel to the Ti–O chain. Our investigations in section 3.2 have demonstrated that only an unrealistic large $\Pi_{O_\parallel}$, i.e. small η, resulted in a FE instability. On the other hand, from our qualitative arguments in context with figures 5(b) and (e) we expect off-site CF to enhance the phonon-induced changes in polarizability and favour ferroelectric behaviour. This conjecture will be examined by means of quantitative calculations in the following. The relevant parameter which measures the localization of the off-site CF centres and thus the scale on which the CT takes place can be defined in terms of the quantity

$$\gamma = \frac{\tau_a}{\tau_{Ti}}, \tag{26}$$

where τ_a refers to the distance of the off-site CF centre δQ_a^{off} (figure 6) from the nearest oxygen ion. τ_{Ti} measures the nearest neighbour distance between oxygen and titanium along the chain. Thus, as shown in figure 6, $\gamma = 0\%$ means that δQ_a^{off} is on oxygen and $\gamma = 100\%$ refers to the case where δQ_a^{off} is on titanium. For symmetry reasons a second centre δQ_b^{off} has to be located on the next Ti–O bond at the same distance from the oxygen. Thus, the one-centre-per-bond model of figure 5(b) can be realized with Q_a^{off} and δQ_b^{off}. Adding δQ_c^{off} and δQ_d^{off} as in figure 6 yields the two-centre-per-bond model of figure 5(e).

Table 5. Values for the model polarizability $\Pi_{\kappa\kappa'}^{\vec{0}\vec{a}}$ calculated according to equation (13) from the tight-binding polarizability, as discussed in the text.

$\Pi_{\kappa\kappa'}^{\vec{0}\vec{0}}$ (meV^{-1})	SrTiO$_3$	BaTiO$_3$
Ti 3d	167.3874	369.4884
O 2s	2.5269	2.6955
O 2p	58.7979	135.7567
Ti 3d–O 2s	−0.9172	−1.2150
Ti 3d–O 2p	−26.9807	−60.3664
O 2s–O 2s	−0.0011	0.0009
O 2p–O 2p	−0.5191	−1.8439
O 2s–O 2p	−0.0391	0.0517
(O 2s–O 2p)$_{on}$	−0.3709	−0.6863

The calculation of the on-site polarizabilities according to the CF–CF submatrix of $\Pi_{\kappa\kappa'}(\vec{q})$ from equation (12) is performed following equation (13), i.e.

$$\Pi_{\kappa\kappa'}^{\vec{0}\vec{0}} = \frac{1}{N_{\vec{0}}}\Pi_{\kappa\kappa'}(\vec{q} = \vec{0}). \qquad (27)$$

Here, a nearest neighbour approximation has been assumed and for the actual calculations the band structures of SrTiO$_3$ and BaTiO$_3$ in the tight-binding parametrization according to [22, 23] are used. From these calculations—see table 5—we find that the diagonal matrix elements Π(Ti 3d–Ti 3d), Π(O 2p–O 2p) and the off-diagonal element Π(Ti 3d–O 2p) dominate by far. The large off-diagonal element reflects the importance of the change of the Ti 3d–O 2p hybridization under perturbation of the system, in particular for BaTiO$_3$, because from our results we see that Π(Ti 3d–O 2p) is more than twice as large for BaTiO$_3$ as for SrTiO$_3$. Similar observations are reported in [7, 19, 25] in context with the calculation of transverse charges in perovskites. In order to guarantee that our modelling is consistent with the charge response of an insulator, the sum rule from equation (14) must be strictly fulfilled. This cannot be true exactly, in a nearest neighbour approximation, so we adapt some of the matrix elements to readjust this sum rule. The off-site CF in our model must also be chosen to obey this sum rule. Fixing $\Pi(a)$ as the diagonal term of the off-site CF centre δQ_a^{off}, and taking $\Pi(a) = -2\Pi(a\text{–O 2p})$, the missing matrix element $\Pi(a\text{–Ti 3d})$ is obtained from the sum rule (14), i.e. $\Pi(a) + \Pi(a\text{–Ti 3d}) + \Pi(a\text{–O 2p}) = 0$.

Our numerical simulations in figures 7 and 8 for SrTiO$_3$ have been performed for the one-centre-per-bond model according to figure 5(b). Remarkably, simulations suppressing DF completely, using CF alone, did not show a FE instability. Thus, contributions from the localized screening mechanism via DF are necessary for the instability. For the calculations shown in figure 7 the calculated isotropic Sternheimer polarizabilities from table 2, i.e. $\eta = 100\%$, are used, varying through γ the localization of the off-site CF centres, while in figure 8 γ ($=20\%$) is fixed and the anisotropy of the DF is varied via η taking the Sternheimer result for $\Pi_{O_\perp}$. At the right-hand end of the horizontal axis the parameters of the model are the same in the two figures. A first inspection of the two figures shows that variations of the parameters γ and η produce almost the same effects. Both increasing the anisotropy of the dipole polarizability and decreasing the distance of the off-site CF centre from the oxygen ion result in FE instability (ν(TO1) $= 0$) for certain critical parameters γ, η. At this point the static dielectric constant ε_0 (equation (20)) diverges and the oscillator strength of the FE mode (Ω_{TO1}^2, according to equation (21)) is very large. Moreover, the magnitudes of the phonon-induced DF, $\delta p_{O_\parallel}$, and the off-site CF, δQ_a^{off}, as calculated from equation (23) reach their maximum values with the electrons moving in phase with the rigid charge shift accompanying
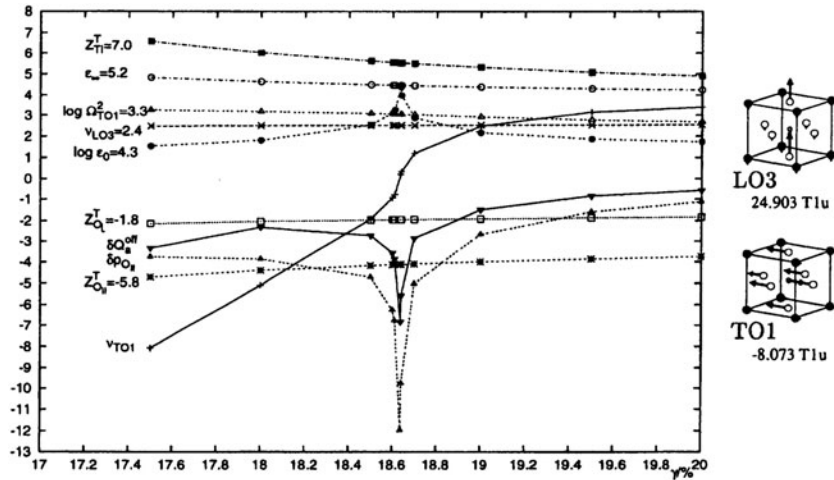
Figure 7. Various physical quantities of SrTiO$_3$ as a function of the localization of the off-site CF centre γ from equation (26) (figure 6), with a fixed ratio η from equation (25) (in per cent) of anisotropy of the dipole polarizabilities $\Pi_{O_\perp}$ and $\Pi_{O_\parallel}$ of oxygen ($\eta = \Pi_{O_\perp}/\Pi_{O_\parallel} = 100\%$). For $\Pi_{O_\perp}$ and $\Pi_{O_\parallel}$ the (isotropic) Sternheimer values of table 2 have been used. The displacement patterns for TO1 and LO3 have been calculated for a fixed $\gamma = 17.5\%$. The experimental results for measurable quantities shown in the figure are explicitly indicated. The behaviours of the following quantities calculated as a function of γ are plotted: frequencies $\nu(\text{LO3})/10$ THz [19], $\nu(\text{TO1})/\text{THz}$; the macroscopic dielectric constant ε_∞ from equation (15) [19]; the static dielectric constant ε_0 from equation (20) [14]; transverse charges Z_α^T from equation (18) [24]; the oscillator strength $\Omega^2(\text{TO1})/\text{THz}^2$ from equation (21) [26]; dipole fluctuations $\delta p_{O_\parallel}/10^{-2}a_B$ from equation (23); off-site charge fluctuations $\delta Q_a^{\text{off}}/10^{-3}$ from equation (23).
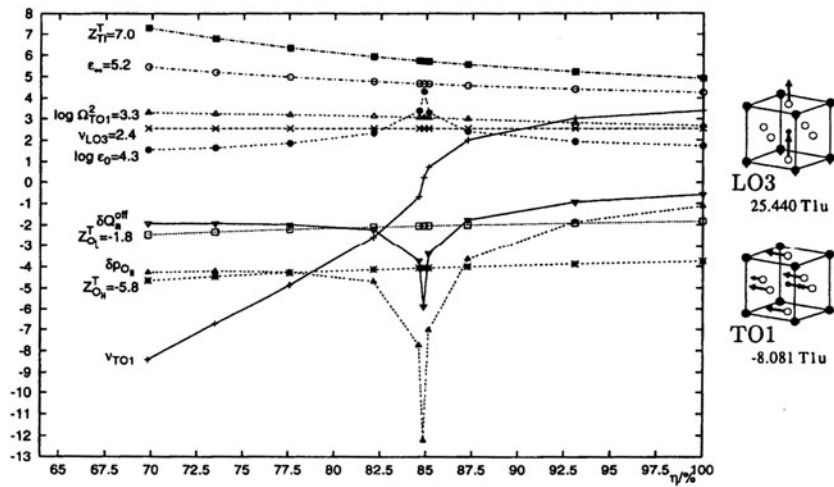

Figure 8. Various physical quantities for SrTiO$_3$, as in figure 7, as a function of η with fixed $\gamma = 20\%$. The displacement patterns have been calculated for fixed $\eta = 70.5\%$. For $\Pi_{O_\perp}$ the calculated Sternheimer value of table 2 has been used.

the displacement of the oxygen ions. In this way, the change of the polarizability is enhanced and the FE transition is generated. As a result we can state that DF and off-site CF interfere constructively to produce the FE instability.
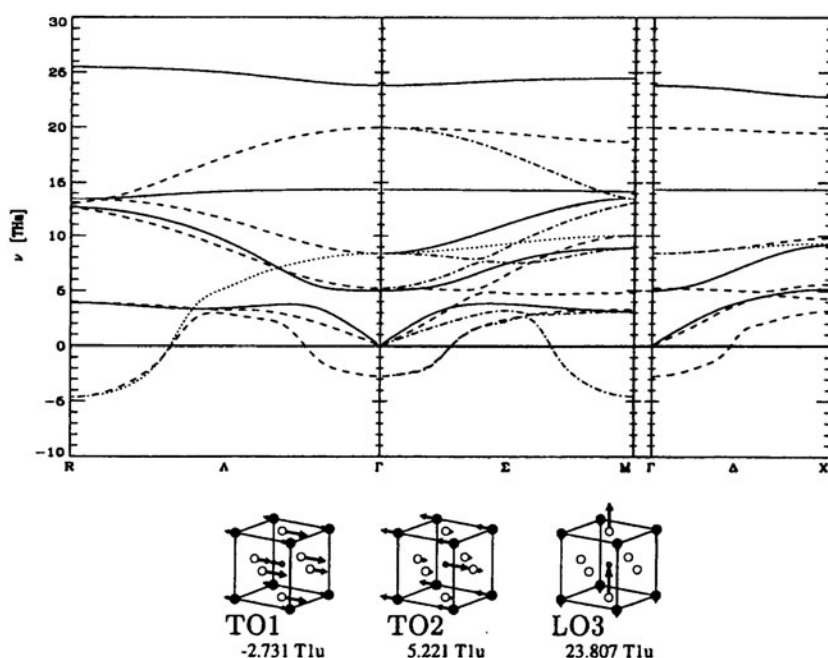
Figure 9. Calculated results for the phonon dispersion of SrTiO$_3$ along the main symmetry directions, as in figure 2, including additionally anisotropic DF and CF as explained in the text (model 3 in table 4).

In the final part of this subsection we present the results for SrTiO$_3$ and BaTiO$_3$ as calculated with the more realistic two-centre-per-bond model (figure 5(e)), taking more realistic dipole polarizabilities $\Pi_{O_\parallel}$ into account. Of course, the insulator sum rules for the charge response have to be satisfied in these calculations. The parameters η and γ have been chosen to give reasonable results for the dielectric properties and the phonon frequencies. The calculated data are collected in table 4 (model 3) and compared with the experiments. The resulting phonon dispersion curves are displayed in figure 9 (SrTiO$_3$) and figure 10 (BaTiO$_3$). For SrTiO$_3$ as well as for BaTiO$_3$ we find FE and AFD instabilities. However, for SrTiO$_3$ the most unstable mode is at R, corresponding to an AFD transition as seen in the experiments, while for BaTiO$_3$ the FE mode at Γ (TO1) is the most unstable, signalling a FE transition, also in agreement with the experimental facts. Moreover, in the case of SrTiO$_3$ the FE instability no longer extends to the zone edges of the Brillouin zone (figure 9) which, however, is the case for BaTiO$_3$ (figure 10) in agreement with recent calculations using DFPT [1]. Thus, the phase space of the ferroelectric instability is reduced in SrTiO$_3$ as compared to BaTiO$_3$. An analogous result has been obtained in [27] by comparing SrTiO$_3$ with ferroelectric KNbO$_3$.

3.4. The phonon density of states, volume effects and FE mode at the Brillouin zone boundary

Figures 11 and 12 display the phonon densities of states of SrTiO$_3$ and BaTiO$_3$ as calculated with model 3 from table 4 corresponding to the phonon dispersion curves shown in figures 9 and 10, respectively. The partial densities of states of the ions Sr(Ba), Ti, O$_\perp$ and O$_\parallel$ are also given and are indicated by different line types. The two most prominent peaks in the spectra relate to the nearly dispersionless part of the branches resulting from the TA, LA and LO2 modes. The main spectrum ends with contributions around the TO3 mode. The part of the
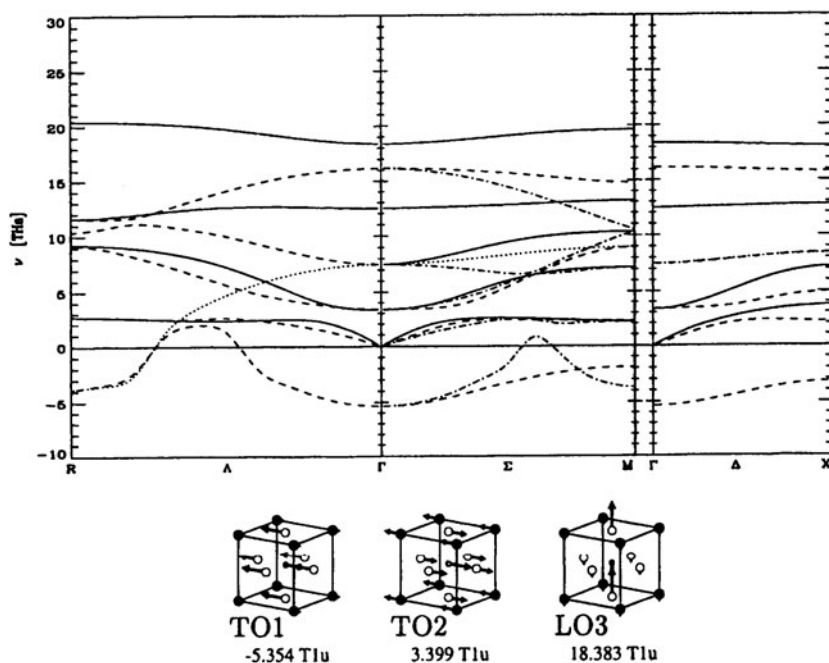
Figure 10. Calculated results for the phonon dispersion of BaTiO$_3$ along the main symmetry directions, as in figure 1, including additionally anisotropic DF and CF as explained in the text (model 3 in table 4).
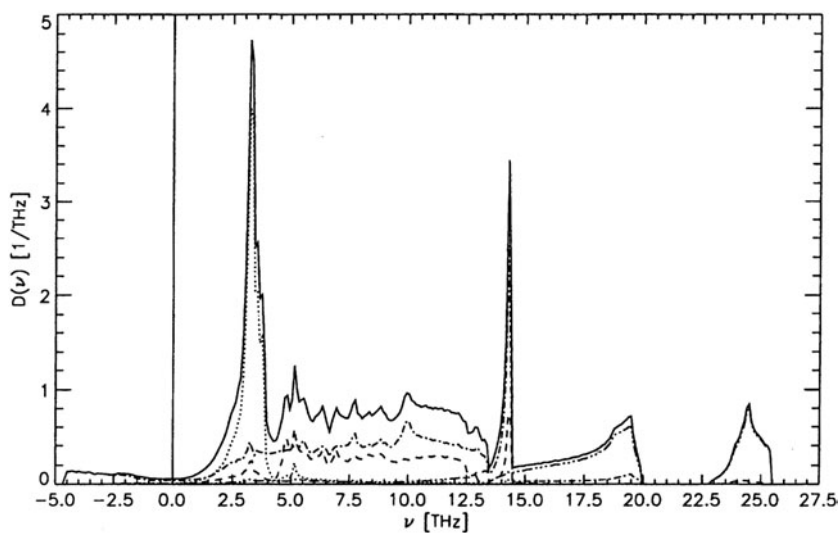

Figure 11. The phonon density of states $D(\nu)$ and partial densities of states $D_\alpha(\nu)$ of SrTiO$_3$ as calculated with model 3 of table 4. The various densities of states are indicated by different line types: ——, $D(\nu)$; · · · · · ·, $D_{Sr(\nu)}$; - - - -, $D_{Ti(\nu)}$; — · —, $D_{O_\perp(\nu)}$; — · · —, $D_{O_\parallel(\nu)}$.

spectrum beyond the frequency gap contains the modes with frequencies starting with LO3 and ends with the (three-dimensional) oxygen breathing mode at the R point which is the highest
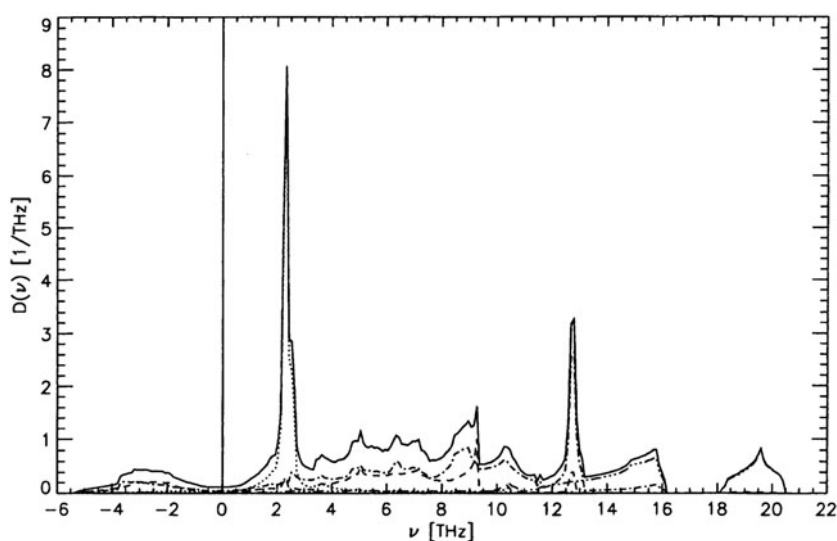
Figure 12. As figure 11, but for BaTiO$_3$.

Table 6. The frequency of the TO1 mode and the R point mode of SrTiO$_3$ in model 3 of table 4 at different lattice constants a. a_0 is the calculated lattice constant at minimal energy from table 1, displayed in the fourth column. SRF(+, −) means that short-range overlap forces are included (+) or excluded (−), respectively. Imaginary frequencies of unstable modes are given as negative numbers.

SrTiO$_3$	SRF(+)		SRF(−)	
a/a_0 (THz)	100%	95%	100%	95%
ν(TO$_1$)	−2.73	4.23	−33.85	−32.37
ν(R)	−4.66	−6.73	7.95	8.60

mode in the spectra, where all the oxygens vibrate in phase against the titanium. Interestingly, in the HTSC, similar modes, the high-frequency Cu–O breathing modes, have been shown to generate a strong electron–phonon coupling when these materials are doped with holes; see e.g. [4, 5] and references therein.

We now briefly address the effect of a compressed cubic structure on the FE mode behaviour. From the results given in table 6 we find that the FE TO1 mode is considerably stabilized under compression in the case where long-range as well as short-range forces are included in the calculation. Such an effect is absent when short-range forces are excluded. In this case the stabilizing effect mediated by the increase of the short-range overlap forces in the compressed structure is switched off and the compression hardly shows any stabilizing effect. The large negative numbers for ν(TO1) of course result from the exclusion of the short-range forces, demonstrating again the favourable aspect of the long-range Coulomb forces for the FE instability. In contrast, the R point mode shows the favourable aspect of the short-range forces for the AFD instability.

As the last topic of this paper, we investigate the behaviour of the FE mode of BaTiO$_3$ along the Brillouin zone boundary. Figure 13 shows a plot of the unstable 'frequency' behaviour and the corresponding displacement patterns of the FE TO1 mode of BaTiO$_3$ in model 3 of table 4 at the Brillouin zone boundary along the Z direction from X $= \pi/a(1, 0, 0)$ to
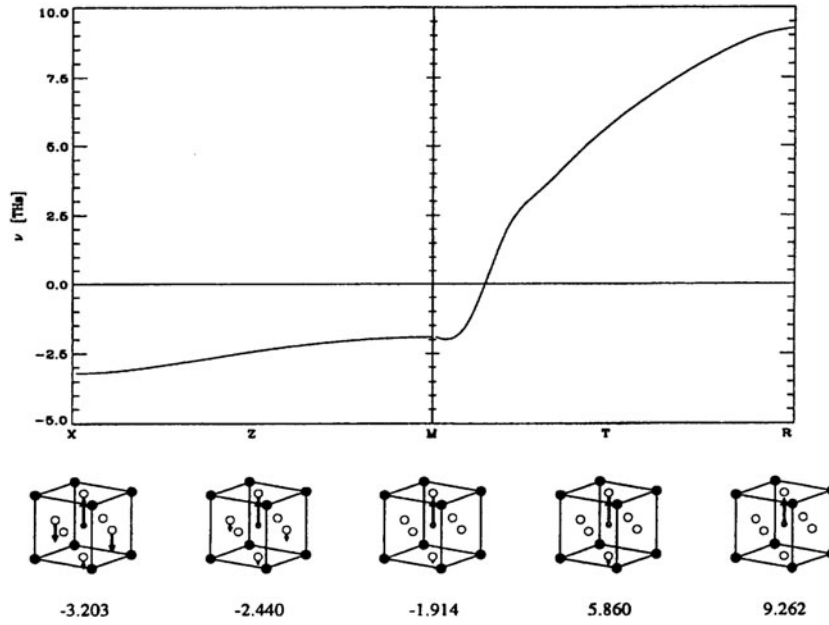
Figure 13. The behaviour of the ferroelectric TO1 mode of BaTiO₃ as calculated with model 3 of table 4, along the Brillouin zone boundary. The displacement patterns are shown from left to right in the following order: X point; halfway from X to M; M point; halfway from M to R; R point. $X = \frac{\pi}{a}(1, 0, 0)$; $M = \frac{\pi}{a}(1, 1, 0)$; $R = \frac{\pi}{a}(1, 1, 1)$.

$M = \pi/a(1, 1, 0)$ and the T direction from M to $R = \pi/a(1, 1, 1)$. It can be seen that the FE instability ($\omega^2(\vec{q}) < 0$) persists along the entire Z direction and disappears along T toward the R point. Taking the results for the instability from figure 10 into account, the FE mode remains unstable on the Γ–M–X plane throughout the whole Brillouin zone. The extension of the region of instability into the third dimension can be extracted from the dispersion in the T direction, where the FE mode is stabilized after roughly 15% when going from M to R. Consequently, the FE mode is unstable between three pairs of flat surfaces containing the Γ point that are parallel to the faces of the Brillouin zone cube. Such a behaviour, found in our microscopic model for BaTiO₃, has been previously reported in [28] for KNbO₃ and later also for BaTiO₃ [29] in the framework of first-principles lattice dynamics calculations and it was pointed out that this behaviour corresponds to chain instabilities in real space. From our calculations along the T direction, the thickness of the slab-like region of instability can be estimated to be about 0.47 Å⁻¹ in reciprocal space. From the displacement patterns in figure 13 we learn that at all points shown the mode is polarized along the z-axis with Ti ions vibrating against the oxygens. At the M point, for example, the unstable mode is dominated by displacements of mostly Ti against the chain oxygen O∥. The phonon phase factor, $e^{i\vec{q}\cdot\vec{R}^{\vec{a}}}$, in the z-direction $\sim(0, 0, 1)$ is one in this case. Thus, the Ti and O∥ ions in the elementary cells will be coherently displaced along an infinite $(0, 0, 1)$ chain. As soon as the $\vec{q}$ vector assumes a z component when going from M to R, the coherence of the displacements will be reduced and a finite length of correlation will be reached when the mode becomes stable along the T direction. So, the minimal correlation length of the displacements for finding an unstable mode can be estimated from our calculation as $2\pi/0.47$ Å⁻¹ ≈ 13.5 Å, which compares quite well with an estimate of 16 Å in [29]. Analogously, these statements hold true for all the

$\vec{q}$ vectors in the Γ–M–X plane with the corresponding modes, because the phase factor along the $(0, 0, 1)$ direction is still one. However, certain differences may occur. For example, at the M point and for $\vec{R}^a = (a, 0, z)$ we have $e^{i\vec{q}_M \cdot \vec{R}^a} = -1$, i.e. two neighbouring chains of elementary cells are oscillating with opposite phase, resulting in a disappearing macroscopic polarization. At the X point and for $\vec{R}^a = (a, y, z)$, $e^{i\vec{q}_X R^a} = -1$ and the coherent chains of elementary cells, as for M, are changed to coherent y–z planes. Finally, the ferroelectric region spreads into all directions in direct space as the $\vec{q}$ vector approaches the Γ point.

4. Summary and conclusions

An approximate description of the electronic density response within a microscopic model, previously used successfully for the high-temperature superconductors, has been applied to the lattice dynamics, dielectric properties and in particular the structural instabilities of the perovskites $SrTiO_3$ and $BaTiO_3$ which crystallize in the parent structure of the HTSC. A comparative study has been performed and reasonable agreement with the experimental evidence has been achieved. In all cases where a comparison of our calculated results with available full first-principles calculations is possible, our findings are consistent with the latter. At the same time, the numerical effort in our approach is considerably reduced, a direct physical interpretation can be given and, if necessary as for the HTSC, an extension to a non-adiabatic charge response is possible.

Starting from an unbiased *ab initio* RIM the influences of DF and CF representing non-rigid localized and delocalized electronic polarization processes, respectively, have been studied explicitly. We have found a larger ion softening of $BaTiO_3$ as compared with $SrTiO_3$ via an enhanced hybridization tending to reduce the overlap repulsion and softening the short-range forces, with the result that ferroelectric behaviour should be enhanced in $BaTiO_3$. However, no FE instability is found in the RIM; only the rotational soft mode related to the AFD transition in $SrTiO_3$ is seen. We also have addressed the favourable aspect of the long-range Coulomb interactions of driving a FE mode and the fact that an increase of the short-range forces favours the AFD transition.

Localized anisotropic DF as well as delocalized polarization processes via off-site CF, simulating changes of the Ti 3d–O 2p hybridization under atomic displacements, interfere constructively in the FE instability. From a calculation of the off-diagonal matrix elements of the electronic polarizability we see that the changes of hybridization are considerably stronger in $BaTiO_3$. A FE transition with DF exclusively is only possible with anisotropic dipole polarizabilities and under the assumption of an unrealistic large oxygen polarizability $\Pi_{O_\parallel}$ along the Ti–O axis. On the other hand, simulations suppressing DF completely and using CF solely did not show any FE instability. Only an intrinsic interplay of the two screening mechanisms generates ferroelectric behaviour in the particular material.

Moreover, our calculations have shown that changing Sr to Ba has profound effects on the character of the phonon dispersion and the unstable modes. In agreement with the experimental situation, our findings extracted from the calculations are that in $SrTiO_3$ the most unstable mode is the rotational mode at R corresponding to an AFD transition, while in $BaTiO_3$ the FE mode at Γ is the most unstable. At the same time, the phase space of the FE instability is greatly reduced in $SrTiO_3$ as compared to $BaTiO_3$. An analogous result has been observed in first-principles calculations by comparing $SrTiO_3$ with ferroelectric $KNbO_3$. In $BaTiO_3$ our studies show that the region of instability lies between three pairs of nearly flat planes which are parallel to the surfaces of the Brillouin zone cube. Such a behaviour has also been reported from full first-principles calculations and it was pointed out that this feature corresponds to

chain instabilities in real space. Besides the phonon dispersion and the dielectric properties, we have also investigated the phonon densities of states with the oxygen breathing mode at the R point at the high-frequency end of the spectra. Similar high-frequency oxygen breathing modes in the HTSC have recently generated a great deal of interest experimentally as well as theoretically, because of the strong electron–phonon coupling of these modes. Finally, we find that the FE instability disappears in the compressed cubic phase.

References

[1] Ghosez Ph, Cockayne E, Waghmare U V and Rabe K M 1999 *Phys. Rev.* B **60** 836
[2] Falter C, Klenner M and Ludwig W 1993 *Phys. Rev.* B **47** 5390
[3] Falter C and Hoffman G A 2000 *Phys. Rev.* B **61** 14537
[4] Falter C and Hoffman G A 2001 *Phys. Rev.* B **64** 054516
[5] Falter C and Schnetgöke F 2002 *Phys. Rev.* B **61** 054510
[6] Falter C, Hoffmann G A and Schnetgöke F 2002 *J. Phys.: Condens. Matter* **14** 3239
[7] Ghosez Ph, Michenaud J P and Gonze X 1998 *Phys. Rev.* B **58** 6224
[8] Harrison W A 1980 *Electronic Structure and the Properties of Solids* (San Francisco, CA: Freeman)
[9] Ghosez Ph, Gonze X, Lambin Ph and Michenaud J P 1995 *Phys. Rev.* B **51** 6765
[10] Falter C, Klenner M, Hoffman G A and Schnetgöke F 1999 *Phys. Rev.* B **60** 12051
[11] Perdew J P and Zunger A 1981 *Phys. Rev.* B **23** 5048
[12] Unoki H and Sakudo T 1967 *J. Phys. Soc. Japan* **23** 546
[13] Shirane G and Yamada Y 1969 *Phys. Rev.* **177** 858
[14] Müller K A and Burkhard H 1979 *Phys. Rev.* B **19** 3593
[15] Müller K A, Berlinger W and Tosatti E 1991 *Z. Phys.* B **84** 277
[16] Zhong W and Vanderbilt D 1996 *Phys. Rev.* B **53** 5047
[17] Cohen R E 1992 *Nature* **358** 136
[18] Nakamura T 1992 *Ferroelectrics* **137** 65
[19] Zhong W, King-smith R D and Vanderbilt D 1994 *Phys. Rev. Lett.* **72** 3618
[20] Servoin J L, Luspin Y and Gervais F 1980 *Phys. Rev.* B **22** 5501
[21] Cohen R E and Krakauer H 1990 *Phys. Rev.* B **42** 6416
[22] Mattheiss L F 1972 *Phys. Rev.* B **6** 4718
[23] Pertosa P and Michel-Calendini F M 1978 *Phys. Rev.* B **17** 2011
[24] Axe J D 1967 *Phys. Rev.* **157** 429
[25] Posternak M, Resta R and Baldereschi A 1994 *Phys. Rev.* B **50** 8911
[26] Kvyatkovskii O E 1997 *Phys. Solid State* **39** 602
[27] Lasota C, Wang C-Z, Yu R and Krakauer H 1997 *Ferroelectrics* **194** 109
[28] Yu R and Krakauer H 1995 *Phys. Rev. Lett.* **74** 4067
[29] Ghosez Ph, Gonze X and Michenaud J P 1998 *Ferroelectrics* **206** 205